Full Length Article

Synthesis of Pt decorated manganese oxide (MnO$_2$/Mn$_5$O$_8$) nanorods and their catalytic activity for the reduction of 4-nitrophenol to 4-aminophenol

Ivan Marić [a], Monika Šoltić [b], Goran Dražić [c], Matthijs A. van Spronsen [d,*], Goran Štefanić [b], Mile Ivanda [b], Georg Held [d], Tanja Jurkin [a], Klemen Bohinc [e], Marijan Gotić [b,*]

[a] Radiation Chemistry and Dosimetry Laboratory, Division of Materials Chemistry, Ruđer Bošković Institute, Bijenička cesta 54, 10 000 Zagreb, Croatia
[b] Laboratory for Molecular Physics and Synthesis of New Materials, Division of Materials Physics, Ruđer Bošković Institute, Bijenička cesta 54, 10 000 Zagreb, Croatia
[c] Department of Materials Chemistry, National Institute of Chemistry, Hajdrihova 19, SI-1001 Ljubljana, Slovenia
[d] Diamond Light Source Ltd, Oxfordshire, United Kingdom
[e] Faculty of Health Sciences, University of Ljubljana, 1000 Ljubljana, Slovenia

ABSTRACT

α-MnO$_2$ nanorods (NRs) were synthesized by microwave irradiation and used as supports for platinum nanoparticles by wet impregnation with Pt(acac)$_2$ as precursor. XRD analysis revealed that the samples without platinum (sample MP0) and with 1 % platinum (sample MP1) contained tetragonal α-MnO$_2$. Samples with 3 % (sample MP3) and 5 % (sample MP5) of platinum contained monoclinic Mn$_5$O$_8$ in addition to α-MnO$_2$, with Mn$_5$O$_8$ dominating in sample MP5. Rietveld analysis showed that the lattice parameters of α-MnO$_2$ increased slightly with Pt loading. SEM and STEM showed that higher Pt loadings resulted in shorter nanorods and different sizes and dispersions of PtNPs on their surface. XPS results showed a decrease in Pt(IV) and Pt(II) concentration with Pt loading, while Pt(0) increased. NEXAFS results showed the presence of Mn(II) in MP3 and MP5, which is consistent with XRD results detecting Mn$_5$O$_8$. The catalytic activity of the Pt/α-MnO$_2$ nanorods was tested in the catalytic reduction of 4-nitrophenol to 4-aminophenol. MP1, with the lowest platinum content, exhibited the highest mass normalized rate constant k_{app}/m_{Pt} of 1.8×10^4 s^{-1} g^{-1}. The study suggests that the presence of Pt(IV) is not a limiting factor for the catalytic reduction of 4-NP to 4-AP.

1. Introduction

The development of highly efficient and selective catalysts for organic reactions, especially for the production of high value-added products, is of paramount importance in various research areas of materials science and catalysis [1]. Heterogeneous catalysts are preferred over homogeneous catalysts because they are recyclable and can be easily separated from the reaction medium [2]. Among the numerous catalytic materials, transition metal oxides have attracted considerable attention due to their exceptional physical and chemical properties and the potential for tailored modifications leading to decorated nanoparticles, nanoarrays, core–shell nanostructures, Janus nanostructures and many more [3–5]. In particular, manganese dioxide (MnO$_2$) is a compelling candidate due to its large surface area, robust stability, and easy accessibility. Moreover, MnO$_2$ can be conveniently synthesized in various morphologies, and the precursor materials are abundant and inexpensive. For example, Xiao et al. synthesized MnO$_2$ in various forms, including microspheres, nanorods, and nanotubes, by simply varying the temperature of the hydrothermal reaction [6]. Similarly, Yu et al. synthesized cocoon-like, urchin-like and nest-like MnO$_2$ nanostructures by wet chemical methods [7]. In general, the catalytic performance of MnO$_2$ nanostructures depends on their morphology, as shown by Wang et al. who found that rod-shaped MnO$_2$ nanoparticles performed better than MnO$_2$ tubes, flowers, and wires in catalysing various reactions [8].

MnO$_2$ and its composites are widely used as catalysts for various chemical reactions, such as the degradation of dyes, pesticides, and antibiotics, and the redox reaction of phenolic compounds, including the conversion of 4-nitrophenol (4-NP) to 4-aminophenol (4-AP) [9,10].

This reaction is used as a model reaction for catalytic reduction for several reasons. 4-NP is a ubiquitous pollutant and the most abundant phenolic compound used extensively in the production of synthetic dyes, herbicides, and active pharmaceutical ingredients [11]. In addition, the final product, 4-AP, is a value-added chemical used as a precursor in the manufacture of analgesics and antipyretics. Finally, this reaction does not produce any by-products, and its kinetics can be easily monitored by UV–Vis spectroscopy [12].

However, the catalytic potential of MnO_2 alone is limited by its modest catalytic activity and selectivity. In an effort to overcome these limitations associated with metal oxide materials, various strategies have been developed, including the decoration of metal oxide supports with noble metals that can significantly improve the catalytic performance of the material, such as palladium [13], silver [14], gold [15], and platinum [16]. Platinum (Pt) is a promising candidate due to its excellent catalytic activity, large surface area, and good stability, as shown by several studies on the Pt-catalyzed reduction of 4-NP [17,18]. Zhou *et al.* synthesized a magnetic Fe_3O_4/SiO_2 hybrid support coated with hyperbranched polyglycerol and decorated with Pt/Au/Pd nanoparticles and demonstrated its effectiveness for the catalytic reduction of 4-NP [19]. In our previous work, we investigated the catalytic efficiency of Pt-decorated SnO_2 and Fe_2O_3 metal oxide supports, highlighting the central role of the strong interaction between these reducible metal oxides and well-dispersed Pt nanoparticles for catalytic activity. Similar observations were made in previous work by other authors, e.g., Wang *et al.* who studied the interaction of Pt nanoparticles with SiO_2, Co_3O_4, MnO_2, Fe_2O_3, NiO, and CeO_2 supports [20]. Although Pt/MnO_2 nanostructures have been explored for various reactions, e.g., water–gas shift [10], as electrocatalysts for $Li\text{-}O_2$ batteries [21], the oxidation of formaldehyde [7,22], and for the determination of pyrocatechol and hydroquinone [23], Pt/MnO_2 has apparently not yet been investigated for the catalytic reduction of 4-NP to 4-AP.

Therefore, the focus of this research is on the synthesis, characterization, and catalytic properties of Pt-decorated MnO_2 nanorods (Pt/MnO_2 NRs). This comprehensive study investigates both the effects of Pt loading and the specific MnO_2 morphology, which has been clearly shown to be excellent for catalytic reactions. MnO_2 was chosen as a support due to its facile synthesis in 1D morphology [24] and its properties as a reducible metal oxide with a rich redox chemistry [25]. Our results clearly confirm that the dispersion, nanoparticle size, and redox state of the Pt species depend on the initial platinum loading. Surprisingly, platinum almost completely converted the tetragonal α-MnO_2 nanorods into monoclinic Mn_5O_8, and while pure MnO_2 nanorods show no catalytic activity in the reduction of 4-NP to 4-AP, the Pt/MnO_2 nanorods exhibit exceptional catalytic activity and selectivity for this conversion. Moreover, the Pt/MnO_2 NRs exhibit commendable stability and reusability, making them promising candidates for use as catalysts in various organic reactions, especially in the conversion of aromatic compounds.

2. Materials and methods

2.1. Chemicals

Potassium permanganate (reagent grade, ACS, ISO, Reag. Ph Eur, Cat. No. PO03311000) produced by *Sharlab*, hydrochloric acid (for trace analysis, fuming, ≥37 %, Cat. No. 101759167) and platinum(II) acetylacetonate (97 %, Cat. No. 282782) produced by *Sigma-Aldrich*, ethanol absolute (99.98 % p.a., Cat. No. p1473) produced by *Gram-Mol* and toluene (p.a., Cat. No. 1914401) produced by *Kemika* were used. All chemicals were of analytical purity and used as received.

2.2. Synthesis procedure

The synthesis of MnO_2 was performed according to a modified procedure by Li *et al.* [24,26]. In a typical experiment, 1.5 mmol of $KMnO_4$

was dissolved in 20 mL of Milli-Q water. To this solution, 0.5 mL of concentrated HCl (37 %) was added dropwise for 20 min under vigorous stirring using a magnetic stirrer. The solution was then transferred to quartz tubes and placed in the Anton Paar Multiwave 5000 microwave reaction system. The reaction temperature was programmed to reach 140 °C as quickly as possible and held for 25 min. After completion of the procedure, the sample was cooled to room temperature and collected through several cycles of centrifugation and washing with deionized water and ethanol. The sample was dried overnight in a vacuum dryer.

For the synthesis of Pt/MnO_2 nanostructures with different molar ratios of Pt on MnO_2, the following procedure was used: 0.2 g MnO_2 was suspended in 30 mL ethanol in an ultrasonic bath. 0.0452 g of Pt(acac)$_2$, 0.0272 g of Pt(acac)$_2$, or 0.009 g of Pt(acac)$_2$ were dissolved in 5 mL of toluene to give Pt/MnO_2 molar ratio percentages of 5 %, 3 %, and 1 %, respectively. The completely dissolved Pt(acac)2 was mixed with MnO_2 suspended in ethanol and stirred to dryness for 3 h using a magnetic stirrer. After mixing, the sample was allowed to dry further overnight in a vacuum. The dried powder was then placed in an oven at 200 °C for 1 h and at 400 °C for 2 h.

The samples are designated as MP0, MP1, MP3, and MP5, where the numbers 0, 1, 3 and 5 represent the molar ratio percentages of Pt on the MnO_2 support.

2.3. Catalysis experiments

The catalytic reduction of 4-nitrophenol (4-NP) to 4-aminophenol (4-AP) was studied by UV–Vis spectrophotometry in the presence of the synthesized samples and $NaBH_4$ [27]. 4-nitrophenol and $NaBH_4$ solutions were not purged with N_2 prior to catalytic measurements. The aqueous $NaBH_4$ solution was freshly prepared before each experiment. In a typical experiment, 0.3 μmol of 4-NP (20 μL of a 0.015 M solution) was added to 3 mL of ultrapure water in a quartz cuvette, then 60 μmol of $NaBH_4$ (20 μL of a 3 M solution) was added to the cuvette. Into the above solution, 20 μL of catalyst (3 mg ml^{-1} in water) was dropped into the quartz cuvette and mixed rapidly with a micropipette, after which the UV–Vis spectra were recorded as a function of time.

Reusability tests were performed using the setup described above. After the first cycle, 20 μL of a 0.015 M 4-NP solution (0.3 μmol) was added to the suspension and mixed rapidly, after which the UV–Vis spectra were recorded in the same manner. This was performed for a total of 5 cycles. Before the third cycle, 20 μL of a 3 M $NaBH_4$ solution (60 μmol) was added in addition to the 4-NP solution to ensure that $NaBH_4$ was present in a large excess.

2.4. Instrumental analysis

X-ray diffraction (XRD) measurements were performed at room temperature using APD 2000 diffractometer (CuKα radiation, graphite monochromator, NaI-Tl detector) manufactured by ITALSTRUCTURES, Riva Del Garda, Italy.

The morphology and elemental analysis of the samples were investigated using the atomic resolution scanning transmission electron microscope (AR STEM), model Jeol ARM 200 CF, with voltage emission of 200 kV coupled with Gatan Quantum ER system and with electron energy loss spectroscopy and energy dispersive x-ray spectrometry (Jeol Centurio 100), as well as the thermal field emission scanning electron microscope (FE-SEM), model JSM-7000F, manufactured by JEOL Ltd. connected to the EDS/INCA 350 (energy dispersive X-ray analyzer) manufactured by Oxford Instruments.

Nitrogen adsorption measurements at 77 K for Brunauer-Emmett-Teller (BET) analysis and necessary degassing pre-treatment were done on Quantachrome Autosorb iQ3 system. Prior to the measurement, the material was kept at 250 °C under vacuum to remove any residual gas and moisture from the sample. This was performed until the rate of rise of pressure with closed vacuum valves was less than 50 millitorr per minute. The adsorption–desorption isotherms were measured at 77 K in

a relative pressure range of ~ 10^{-5} to ~ 0.99.

X-ray photoelectron spectroscopy (XPS) data were collected using a Thermo NEXSA system equipped with a monochromatic Al-K$_\alpha$ source. Samples were pressed into carbon tape stuck on Al foil clamped to a stainless-steel sample plate. Per sample, one spot of 0.4 mm was analysed by recording the Pt4f, Mn2p, O1s, and C1s regions (the set of single iterations was repeated 10 times), after which a survey was recorded. The survey was measured with a pass energy of 200 eV and 10 ms dwell time per data point, the others with 50 eV and 50 ms. The base pressure of the analysis chamber was 2×10^{-9} mbar, increasing to $(4-5) \times 10^{-7}$ mbar during data collection. The spectra were collected with normal emission and the angle between X-ray source and analyser equal to the magic angle. A flood gun was used to minimize the effect of charging. No effort has been made to "calibrate" or reference the binding energy. Details on the fitting of the XPS spectra are given in the Supplementary Information document [28–31].

X-ray absorption spectroscopy was performed on beamline B07C of the Diamond Light Source [32]. The samples were mounted in a similar fashion as for the XPS measurements and loaded in the "TPOT" endstation. The samples were measured at room temperature in 1 mbar of He to mitigate the effect of charging on the spectra. The signals were collected on the cone of the differentially pumped hemispherical analyser. The sample-cone distance was around 0.2–0.3 mm, and the cone was biased at + 5 V, connected to an SRS 570 preamplifier (5 nA/V, low-noise mode, 12-dB low-pass filter set tot 30 Hz). The beamline was operated using a plane-grating monochromator with spacing of 600 lines/mm (c_{ff} of 2) and the exit slits set to 25 μm (energy-dispersive direction) by 0.5 mm, leading to an approximate resolution of 0.16 eV and a beam size of 60 μm × 90 μm (vertical × horizontal) of horizontally, linearly polarized light. The incidence angle was 30 with respect to the surface and the surface was normal to the axis of the analyser.

The X-ray absorption spectra were divided by the I$_{zero}$ current to account for fluctuations in photon flux. This I$_{zero}$ signal, the drain current to an Au mesh in the beam path upstream from the endstation, was measured simultaneously with the spectra. A line fitted to the pre-edge

background was subtracted from the data, after which the spectra were normalized to a point above the edge (660 eV).

Raman spectra were recorded with Renishaw InVia Raman spectrometer using 532 nm laser excitation of 2mW laser power focused with 50x microscope objective.

A Cary Varian 50 Bio UV–Vis spectrophotometer in a wavelength range from 600 to 200 nm and quartz cuvettes with optical path of 1 cm were used in catalytic measurements.

3. Results

Fig. 1 shows the XRD patterns of the synthesized samples. The XRD patterns of samples MP0 and MP1 perfectly match the patterns of tetragonal α-MnO$_2$ (ICDD card 44–141, space group $I4/m$). Sample MP3 also matches well with α-MnO$_2$, along with the pattern of monoclinic Mn$_5$O$_8$ (ICDD card 39–1218, space group $C2/m$), while the diffractogram of sample MP5 can be assigned to α-MnO$_2$, Mn$_5$O$_8$ and cubic platinum (ICDD card 4–802, space group $Fm\bar{3}m$). The volume fractions of α-MnO$_2$ and Mn$_5$O$_8$ in samples MP3 and MP5 were determined by Rietveld refinement using the program MAUD [33–35] (Fig. S1 in the Supplementary Information). The results of the Rietveld refinement showed that the volume fraction of Mn$_5$O$_8$ in samples MP3 and MP5 was 0.39 and 0.64, respectively (Table 1). The values of the unit cell parameters of the α-MnO$_2$-type solid solutions obtained from the results of the Rietveld refinements are shown in Table 2. The effect of platinum

Table 1
The results of phase analysis as determined from Rietveld refinement of the samples MP0, MP1, MP3, and MP5 (performed with MAUD software).

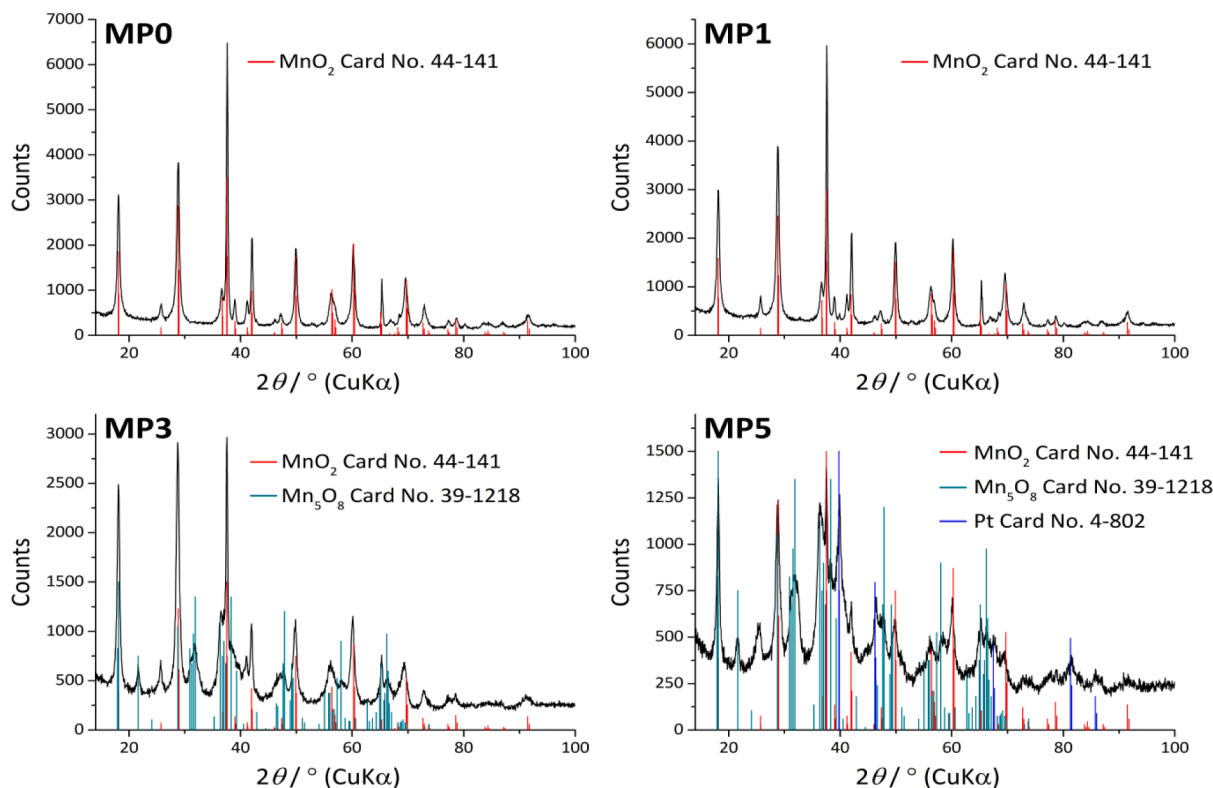| Sample	n(Pt)	Phase composition (volume fraction)
MP0	0	MnO$_2$
MP1	0.01	MnO$_2$
MP3	0.03	α-MnO$_2$ (0.61) + Mn$_5$O$_8$ (0.39)
MP5	0.05	Mn$_5$O$_8$ (0.64) + α-MnO$_2$ (0.35) + Pt (0.01)

Fig. 1. XRD patterns and corresponding assignments of phases for samples MP0, MP1, MP3, and MP5.

Table 2
Refined values of unit-cell parameters *a* and *c*, as well as volume *V*, of the α-MnO2-type solid solutions as determined from the results of Rietveld refinements (program MAUD).

Sample	Lattice parameters of α-MnO$_2$		
	a / nm	*c* / nm	*V*/nm^3
MP0	0.98249(11)	0.28575(3)	0.27583(9)
MP1	0.98352(8)	0.28610(2)	0.27674(6)
MP3	0.98579(6)	0.28657(3)	0.27848(6)

loading on the lattice parameters *a* and *c* and the unit-cell volume of the α-MnO$_2$ is shown in Fig. S2 in the Supplementary Information. The lattice parameters of α-MnO$_2$ increase slightly with Pt loading. The lattice parameters of α-MnO$_2$ as a minor phase in sample MP5 could not be determined because of the very broad maxima.

The results of individual profile fitting indicate the presence of size anisotropy with significantly narrower diffraction lines along the *c*-axis (diffraction line 002) compared to the other directions (Fig. 2). The volume-averaged domain size (D_v) and the upper limits of the microstrains (*e*) were estimated in the direction parallel to the *a*-axis (diffraction lines 200, 400, and 600) from the results of the Williamson-Hall analysis [36] (Fig. 2b) using the equation:

$$\left(\frac{\beta \cos \theta}{\lambda}\right) = \frac{K}{D_v} + \left(\frac{4e\sin\theta}{\lambda}\right) \tag{1}$$

where λ is the wavelength, θ is the Bragg angle, β represents the physical broadening of the diffraction line, and *K* is a constant close to 0.9. The β-values were obtained by a convolution fitting approach (program SHADOW [37]), in which the instrumental profile (diffraction lines of highly crystalline zincite powder [38]) is convoluted with a refinable Voigt function to fit the observed profile.

Fig. 3 shows SEM images of the samples. Long, well-formed nanorods are clearly visible. With increasing Pt content, the length of the rods decreases significantly, from ∼ 3–4 μm for MP0 to ∼ 1 μm for the MP5 sample. Very small dots characteristic of PtNPs are only visible on the microscopic image of the MP5 sample.

Fig. 4 shows the STEM dark-field micrographs of samples MP1 to MP5 at various magnifications and the corresponding size distributions of the Pt nanoparticles. The Pt nanoparticles are homogeneously dispersed on the surface of the nanorods. The mean size of Pt nanoparticles was the smallest in sample MP1 (1.3 nm ± 0.4 nm). In sample MP3 the mean size was 2.6 nm ± 1.2 nm, while in sample MP5 there are two separate distributions of ultrasmall and larger PtNPs. Their mean

sizes were 2.0 nm ± 0.6 nm and 14.5 nm ± 1.3 nm, respectively.

Fig. 5 shows STEM images of samples MP1, MP3, and MP5 and the corresponding EDXS elemental mapping images of the Mn K edge (a, e, i), O K edge (b, f, j), Pt M edge (c, g, k), and the superposition of the three (d, h, l). The green colour represents the Pt M edge, and the small dots on the surface of the nanorods correspond to platinum nanoparticles.

Fig. 6 shows Raman spectra of the synthesized samples. Sample MP0 is characterized by Raman bands at 183, 383, 509, 574, and 631 cm^{-1}. These Raman bands belong to the Mn-O lattice vibrations within the octahedral MnO$_6$ double chains in a tetragonal hollandite-like framework and fit very well with the observed Raman bands of α-MnO$_2$ nanorods reported by Gao *et al.* [25]. Sample MP1 has a very similar Raman spectrum to sample MP0, which is consistent with the XRD results showing that these two samples are single-phase, *i.e.*, consist only of α-MnO$_2$. The Raman spectra of samples MP3 and MP5 show new bands at 171, 264, 475 and 644 cm^{-1}, while other bands shift their positions slightly. The weak band at 264 (ν2) and 475 (ν6) and the very strong band at 644 (ν10) cm^{-1} are characteristic of Mn$_5$O$_8$ nanorods [39]. The most intense Raman band at about 647 cm^{-1} was assigned by Gao *et al.* [25] to an A$_g$ mode originating from the Mn-O vibrations, and this band provides clear evidence that the samples contain Mn$_5$O$_8$.

The Pt4f XPS region recorded for samples MP1, MP3, and MP5 shows the presence of Pt(II) and Pt(IV) for all samples and metallic Pt for samples MP3 and MP5 (Fig. 7). The spectrum for sample MP1 showed two major peaks at 74.5 eV and 77.9 eV assigned to the Pt4f$_{7/2}$-Pt4f$_{5/2}$ doublet of Pt(IV). Additionally, there is a smaller peak at 72.5 eV and a shoulder at 75.9 eV assigned to the doublet of Pt(II). As such, the spectrum could be accurately fitted with a model containing these two species, and the presence of a significant amount of metallic Pt was excluded. To fit the other two spectra, a third component had to be added accounting for the (increasing) presence of metallic Pt (71.2 eV). The fitting improved after allowing the Pt(0) positions with respect to the oxidized Pt species to change between samples MP3 and MP5. This resulted in a + 0.08-eV shift of the Pt(0) in sample MP5 (as referenced to the corresponding oxidized Pt peaks), which could stem from a negative core level shift of smaller Pt nanoparticles observed in sample MP3 (Fig. 4).

The amount of Pt(0) increased linearly with Pt loading (Fig. 8a). Correspondingly, the concentration of oxidized Pt species decreases with increasing the Pt loading, however not monotonously. Increasing the Pt loading from 1 % to 3 % led to a strong reduction in Pt(II) species, while staying roughly similar between 3 % and 5 %. For Pt(IV), on the other hand, the biggest decrease was between Pt loadings of 3 % and 5 %. These general trends were rather independent of the asymmetry
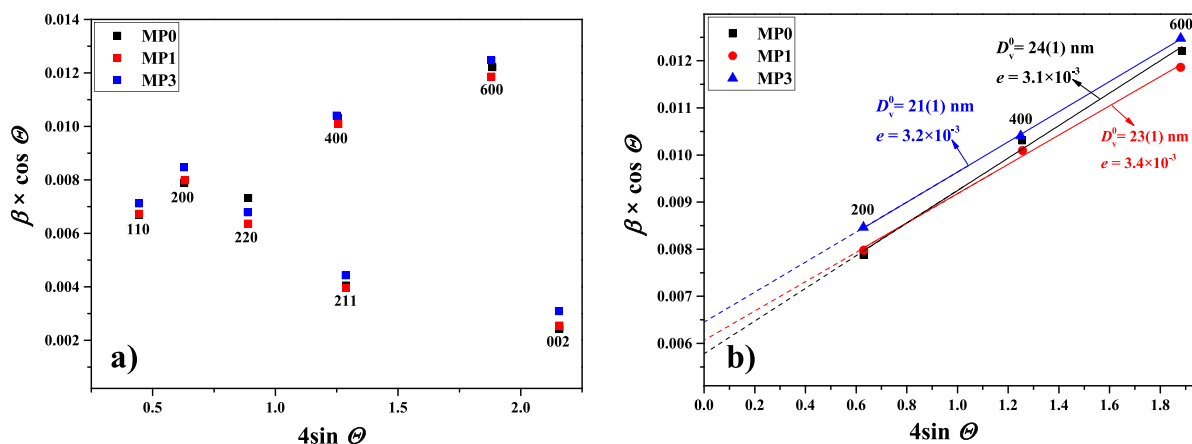

Fig. 2. The results of the diffraction line broadening analysis of the α-MnO$_2$ phase in the X-ray diffraction patterns of samples MP0, MP1, and MP3. Fig. 2a shows the Williamson-Hall plot of the most prominent well separated diffraction lines of α-MnO$_2$ in samples MP0, MP1 and MP3, while Fig. 2b shows the Williamson-Hall analysis of the diffraction lines of α-MnO$_2$ in samples MP0, MP1 and MP3 along the direction < *h*00> (lines 200, 400 and 600) used to estimate the volume-averaged domain size (D$_v$) and the upper limits of microstrains (e) in the direction parallel to the a-axis.
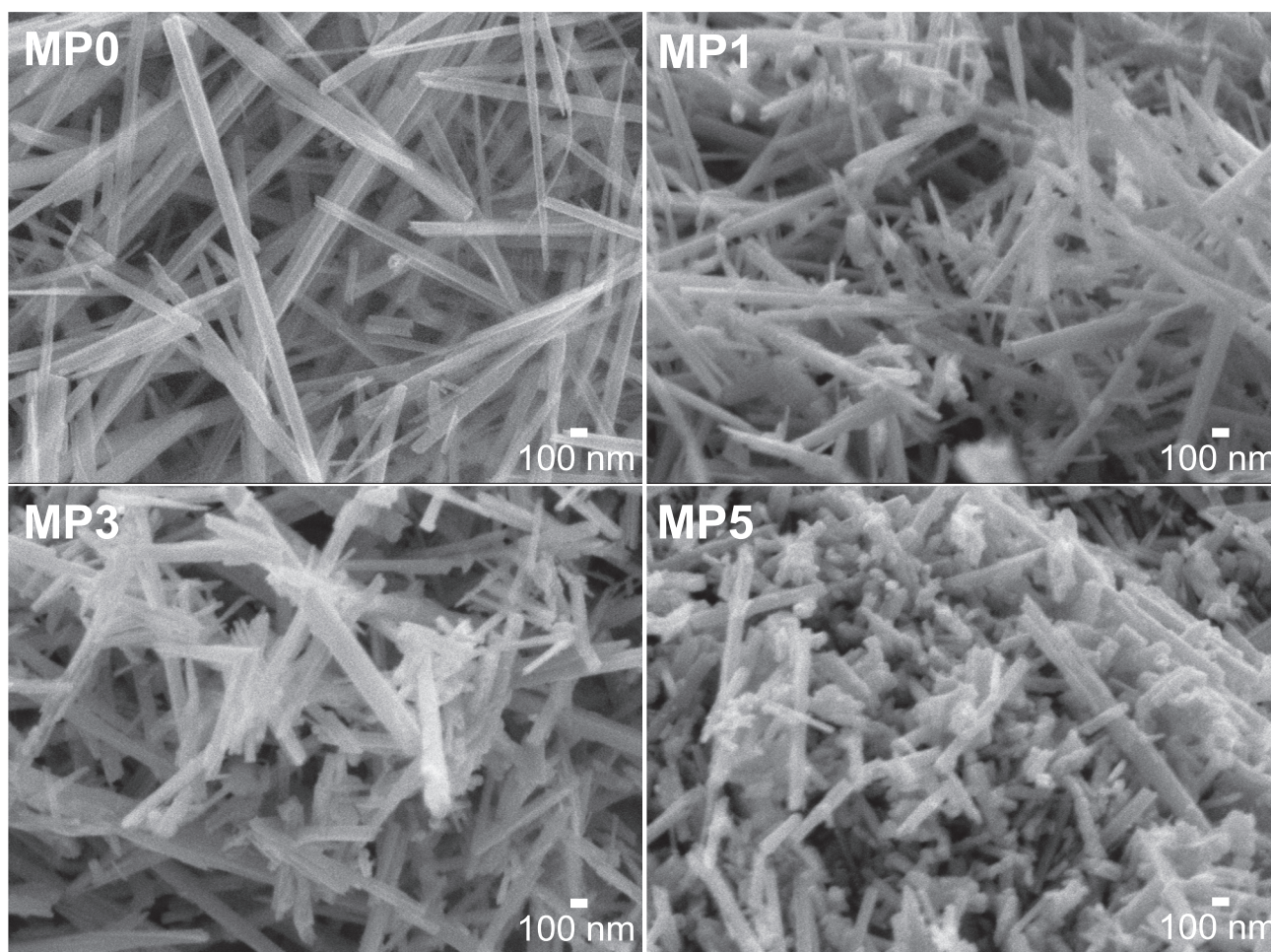
Fig. 3. SEM micrographs of samples MP0, MP1, MP3 and MP5.

parameter used to fit the Pt(0) species.

Importantly, the ratio of the Pt4f/Mn2p peak areas did not show a direct correlation with the nominal Pt loading (black, Fig. 8b), which is most obvious when comparing samples MP3 and MP5. Clearly, the Pt4f/Mn2p ratio decreased even though ICP and EDX showed the Pt loading to increase.

Focusing on the Mn2p region (Fig. 9 and Fig. S9, the Mn2p$_{3/2}$ peak of sample MP0 was fit with 6 fits to account for the multiplet splitting of Mn(IV) and one peak at a position of − 1.1 eV with respect to the first Mn (IV) peak (*cf.* 641.9 and 640.8 eV) [10,31] . This peak is in the work by Biesinger *et al* assigned to Mn(III) [31]. A significant amount (15 %) of Mn(III) was found on the surface of MP0, which is in line with the results reported by Biesinger *et al.* [31]. It should be noted that this fitting model disregards any possible multiplet splitting of the Mn(III) peak. Therefore, the real Mn(III)/Mn(IV) may well deviate from this value. Also, unambiguous assignment of this peak to Mn(III) is difficult given the complicated nature of the Mn2p peaks and the possibility of having a mixture of (hydro)oxides. The same fitting model can be used to fit the Mn2p$_{3/2}$ spectra of samples MP1 and MP5 well. The Mn(III) concentration increases only slightly with Pt loading: 18 % and 19 %, respectively, resulting in a higher full width at half maximum (FWHM) for the measured Mn2p$_{3/2}$ peak, increasing from 2.6 eV for MP0 to 2.8 eV for MP1 and MP5 (Fig. 8b).

However, for sample MP3, a new component had to be added at 640.0 eV (−1.9 eV shifted from the main Mn(IV) peak). The new feature can be attributed to Mn(II). In fact, as the spectra of MnO show a strong peak at 641 eV [31], the peak assigned to Mn(III) likely corresponds to a significant fraction of Mn(II), hence explaining the small shift in this

peak position by + 0.2 eV to 641.0 eV (−0.9 eV with respect to the main Mn(IV) peak). The appearance of Mn(II) lowers the Mn(IV) fraction to 67 %. As a result, the FWHM of sample MP3 is the highest at 3.2 eV (Fig. 8b).

As the Mn2p region is notoriously difficult to fit reliably because of multiplet and charge transfer splitting, the Mn L$_{2,3}$ X-ray absorption edge was measured in conjunction to study the near surface region of the MnO$_2$ rods (Fig. 10). The Mn L$_{2,3}$ edge of α-MnO$_2$ (sample MP0) has two peaks: a narrow one at 640.6 eV and a much broader one at 643.1 eV, while the L$_2$ edge appears as a single broad peak, centred at 653.3 eV. This is consistent with previously reported spectra for MnO$_2$ [40]. A 1 %-Pt loading hardly affects the Mn L$_{2,3}$ spectrum, although it did have a small effect on the FWHM of the Mn 2p$_{3/2}$ XPS peak (Fig. 8b). This can be explained by XPS being more surface sensitive compared to XAS. The former depends on the inelastic mean free path of the photoelectrons, while for the latter, measured in electron yield, elastically and inelastically scattered electrons contribute to the signal.

For the samples with higher Pt loadings, there is a progressive change in the spectra with a small peak appearing at 639.8 eV and some spectral intensity between the α-MnO$_2$ peaks. These spectra resemble the previously published spectrum of Mn$_5$O$_8$ [41]. To highlight the changes, difference spectra have been calculated by subtracting the spectrum for α-MnO$_2$ from the spectra of sample MP3 and MP5 after scaling the α-MnO$_2$ spectrum, such that the spectra do not decrease below the baseline (Fig. 10b). The difference spectrum is larger for MP5 than for MP3, indicating a larger reduction of the α-MnO$_2$ in the MP5 sample. Moreover, the difference spectrum resemble those of Mn(II) in MnO [40,41].
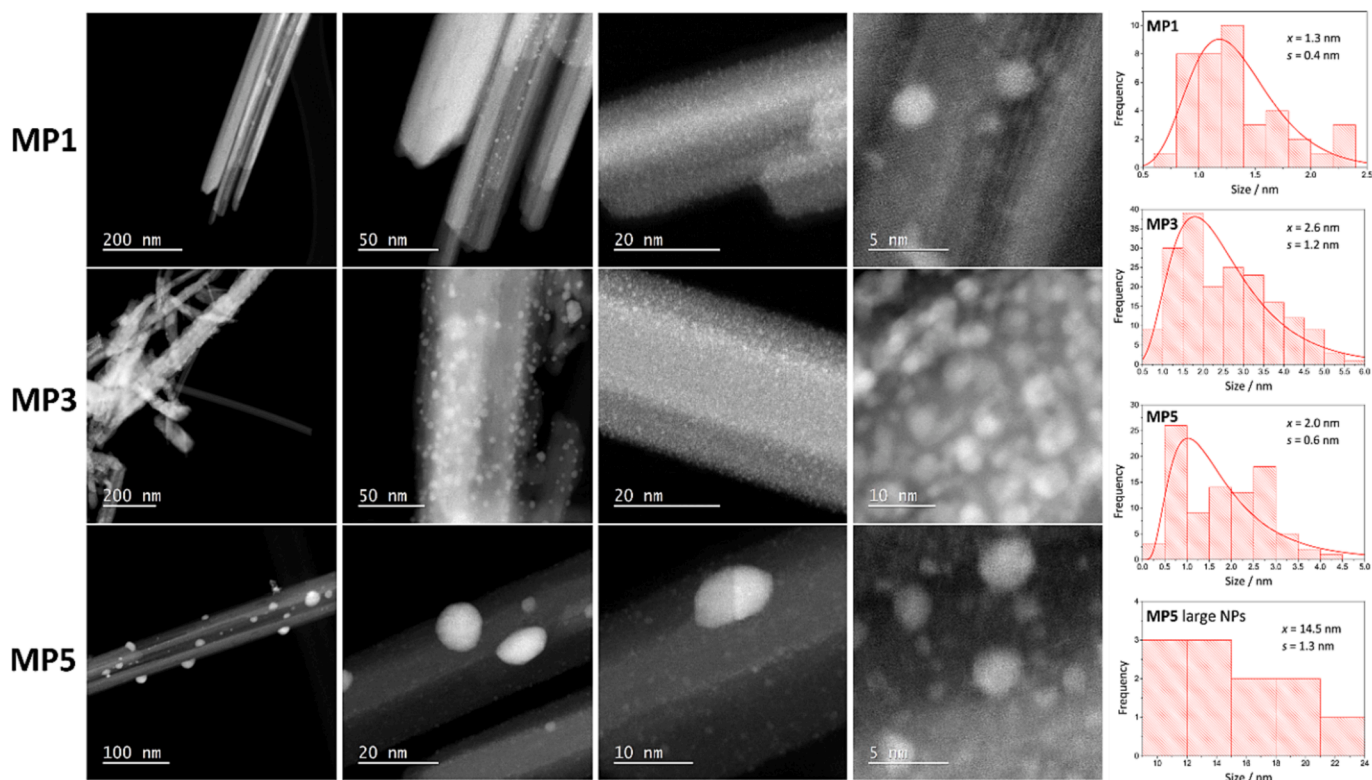
Fig. 4. STEM dark-field micrographs of samples MP1, MP3, and MP5 and their corresponding size distributions, means and standard deviations of Pt nanoparticles.

For the purposes of testing the catalytic efficiency of the samples, 0.06 mg of catalyst was added to the reaction mixture (20 μL of an aqueous catalyst suspension of 3 mg mL^{-1}). Thus, the amount of Pt in the catalysts was 1.4, 4.0, and 6.7 μg for samples MP1, MP3, and MP5, respectively (Table S7, also see Supplementary Information for detailed information on the calculations). For all samples containing Pt, the reaction was complete within 3.5 min, while for the reaction with sample MP0 (without Pt), the absorbance maximum at 400 nm did not decrease significantly (Fig. 11). Moreover, as can be seen from the UV–Vis spectra, there was no induction time for the onset of the reaction. The apparent rate constant of reduction from 4-NP to 4-AP was calculated assuming pseudo-first order kinetics (Fig. 11 inset). Table 3 contains the calculated apparent rate constants, mass-normalized rate constants, and mass- and reaction volume-normalized rate constants.

The recyclability of the catalysts was also tested. All catalysts showed excellent performance during 5 catalytic cycles and completed the reaction in each cycle (Figs. S11, S12, and S13). Although the catalysts performed well in 5 catalytic cycles, there was a visible decrease in the apparent rate constant (Fig. 12). The k_{app} values decreased from 2.5 × 10^{-2} s^{-1} to 5.0 × 10^{-3} s^{-1} for sample MP1, from 3.4 × 10^{-2} s^{-1} to 4.3 × 10^{-3} s^{-1} for sample MP3 and from 4.9 × 10^{-2} s^{-1} to 7.4 × 10^{-3} s^{-1} for sample MP5.

4. Discussion

In this work, α-MnO$_2$ nanorods (NR) were synthesized by microwave irradiation starting from a KMnO$_4$ precursor. Microwave synthesis has several advantages over conventional synthesis methods, such as selective heating of the reactants without heating the entire reaction vessel, which increases the reaction rate and greatly improves energy efficiency. In the present case, using microwave irradiation shortened the synthesis from 14 h in an autoclave from our previous publication [24] to 25 min. The microwave-synthesized α-MnO$_2$ NRs (sample MP0) were used as supports to disperse the platinum catalyst. For this purpose, a Pt(acac)$_2$ precursor was used, which was completely dissolved in

toluene and further diluted in ethyl alcohol. The prepared solution was used for wet impregnation of Pt on powdered α-MnO$_2$.

Although the platinum was impregnated on the surface of α-MnO$_2$ NRs, XRD results showed a new phase, Mn$_5$O$_8$, in samples MP3 and MP5. The formation of this phase was also confirmed by electron diffraction (Fig. S6). Rietveld analysis showed that the volume fraction of Mn$_5$O$_8$ in sample MP3 is 0.39, while in sample MP5, Mn$_5$O$_8$ is the dominant phase with a volume fraction of 0.64. Gao *et al.* [25] prepared Mn$_5$O$_8$ by topotactic conversion of a γ-MnOOH nanorod precursor in nitrogen at 400 °C. In this work, the tetragonal α-MnO$_2$ NRs were converted to monoclinic Mn$_5$O$_8$ by Pt loading, *i.e.*, by adding Pt(acac)$_2$ and heating in air at 400 °C. Therefore, in this work, the transition from α-MnO$_2$ to Mn$_5$O$_8$ involves the rearrangement of the crystal structure from tetragonal α-MnO$_2$ to monoclinic Mn$_5$O$_8$. In addition to the presence of Mn$_5$O$_8$, sample MP5 contains sufficiently large Pt crystals that can be seen in the XRD pattern (Fig. 1). The unit-cell parameters of the α-MnO$_2$ NRs increased slightly and linearly with Pt loading (Fig. S2 and Table 2). Although the exact reason for the increase in unit-cell parameters is not known, the reason could be a reduction of Mn(IV) to Mn(III) and Mn(II). The formation of Mn(III) and Mn(II) with a much larger ionic radius than Mn(IV) could increase the unit cell parameters.

SEM results show that with higher Pt loading, the nanorods become shorter, from 3 to 4 μm in sample MP0 to ∼ 1 μm in sample MP5. STEM results showed that the distribution and size of PtNPs on the surface of α-MnO$_2$ NRs also depend on Pt loading. In samples MP1 and MP3, the PtNPs are homogeneously dispersed on the surface of the MnO$_2$ support with sizes of 1.3 and 2.6 nm, respectively. In sample MP5, both small PtNPs with a size of 2.0 nm and large PtNPs with a size of about 14 nm are present. The results of STEM are in agreement with the XRD analysis, as the PtNPs up to a size of 3 nm are not visible in XRD, while large PtNPs (large Pt crystals) show Pt maxima in the XRD patterns (sample MP5, Fig. 1). The EDXS images of samples MP1, MP3 and MP5 also show that the small PtNPs (represented with green colour in Fig. 5) are homogeneously dispersed on the surface of MnO$_2$.

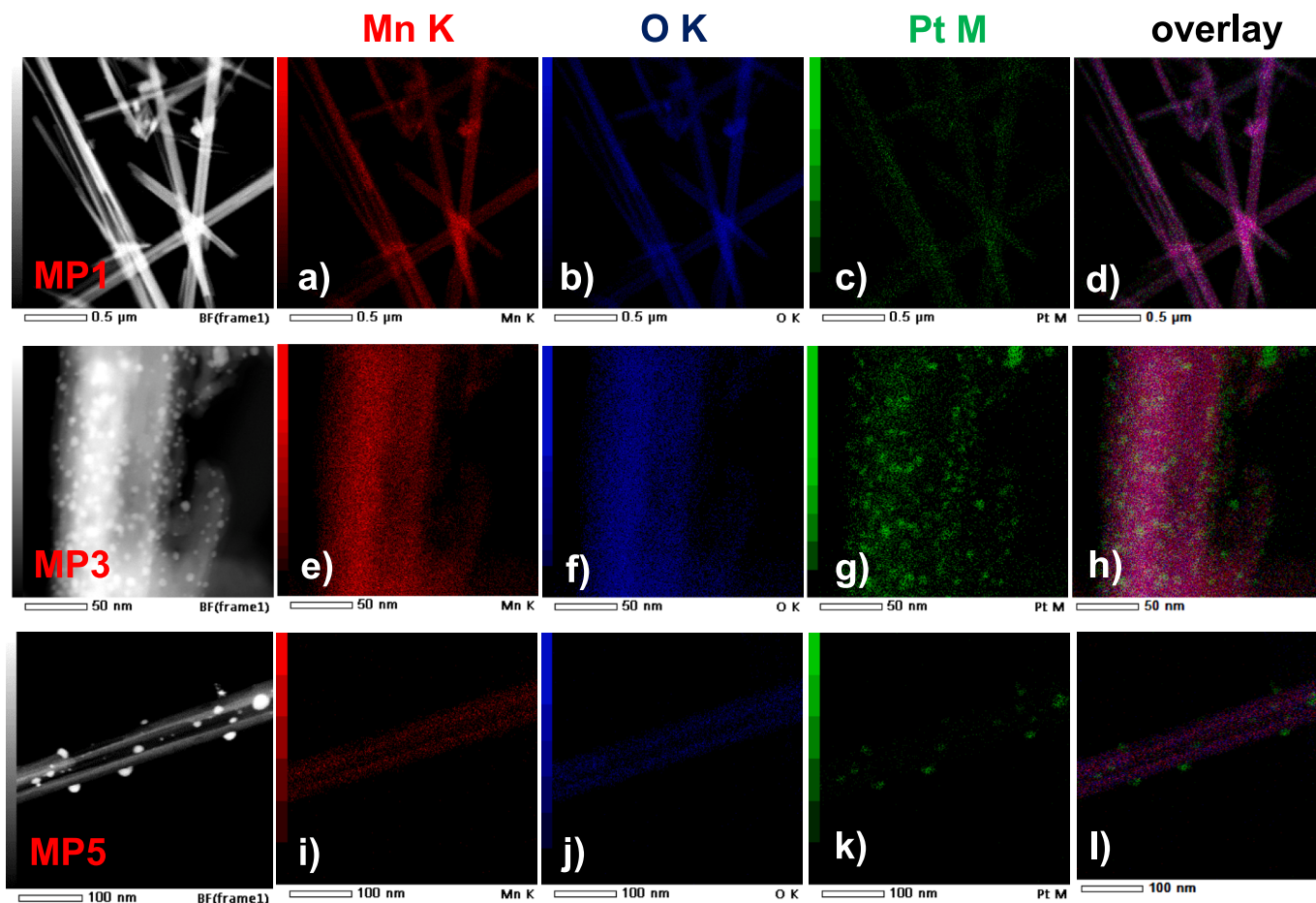The XPS results (Fig. 7) show that the relative concentration of Pt(IV)

Fig. 5. STEM image of sample MP1 (top row), MP3 (middle row) and MP5 (bottom row) and the corresponding EDXS elemental maps of the Mn K edge (a, e, i), O K edge (b, f, j), Pt M edge (c, g, k), and the overlay of the Mn K, O K, and Pt M edges (d, h, l).
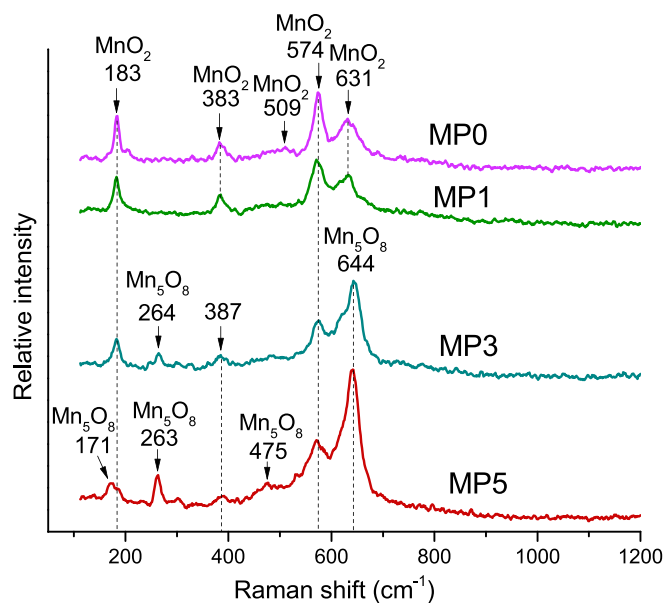

Fig. 6. Raman spectra of samples MP0, MP1, MP3 and MP5.

and Pt(II) in the samples decreases with Pt loading and vice versa for Pt (0), whose relative concentration increases with Pt loading. The sample MP1 does not contain Pt(0). The higher relative concentration of Pt(0) with platinum loading is consistent with the higher relative concentration of Mn(III) and Mn(II) in samples MP3 and MP5 and can be explained by the higher concentration of acetylacetonates derived from the Pt(acac)$_2$ precursor. Mn L$_{2,3}$ edge NEXAFS results (Fig. 10) showed the presence of Mn(II) in samples MP3 and MP5, which is consistent with the XRD results that find Mn$_5$O$_8$ (Mn$_2^{2+}$Mn$_3^{4+}$O$_8$.) in these samples.

Furthermore, a clear increase in Mn2p$_{3/2}$ FWHM was observed with Pt loading (red, Fig. 9). Without Pt, the Mn2p$_{3/2}$ exhibited a FWHM of 2.60 eV, increasing with 0.23 eV and 0.56 eV for samples MP1 and MP3. So, even the smallest loading of Pt has an effect on the MnO$_2$. This is due to reduction of MnO$_2$ by the products of the Pt(acac)$_2$ decomposition. Given that for sample MP1, no reduced Mn species were present in the XRD pattern, the reduction is more pronounced at the surface of the MnO$_2$ rods, as XPS shows an increase in Mn with lower oxidation states between samples MP0 and MP1. Sample MP3 exhibited a significant fraction of Mn(II), indicating that the Mn$_5$O$_8$ was also present at the surface.

Importantly, the Mn(II) fraction disappeared for sample MP5 in XPS, even though NEXAFS and XRD indicate a higher degree in reduction. This can be related to the dewetting observed by SEM and TEM (Figs. 4 and 5) for sample MP5. This may expose some of the reduced Mn to O$_2$ during the annealing step. Therefore, the Mn reduction degree at the surface, as measured by XPS, seems a balance between the reduction by the acetylacetonate decomposition products and by sintering of the Pt nanoparticles and reoxidation of the exposed Mn.

Although the exact mechanism of the formation of Pt(0) and Mn(II) is not known, it can be assumed that the decomposition of acetylacetonate in the presence of two catalysts such as MnO$_2$ and Pt can promote the formation of various carbon compounds including CO gas and small
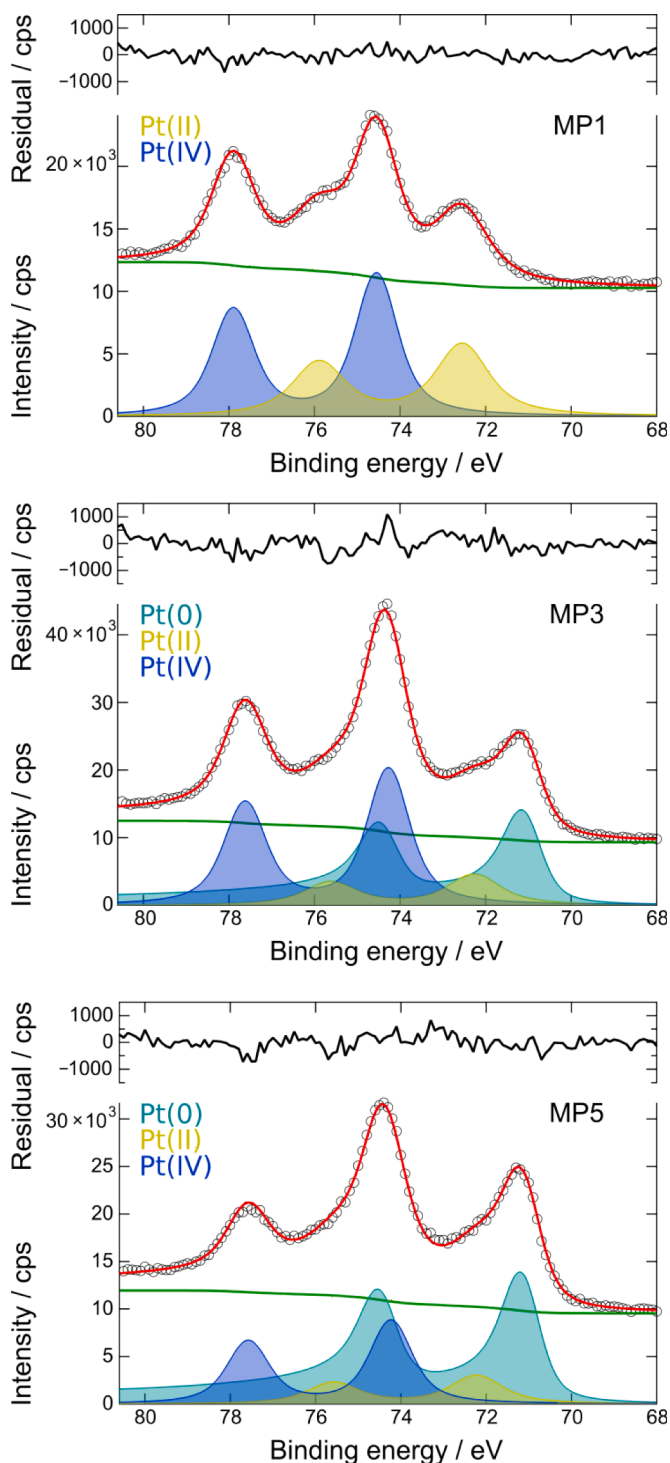
Fig. 7. Pt4f$_{7/2}$-Pt4f$_{5/2}$ XPS of samples MP1, MP3, and MP5. The corresponding XPS survey scans for these samples (and for MP0) can be found in Fig. S10.

carbon nanoparticles, which are intermediate reducing agents and can reduce Mn(IV) and Pt(II) to their lower oxidation state. For example, Kulbakov *et al.* [42] studied the synthesis of PtNPs using Pt(II) acetylacetonate by thermal decomposition. It was found that controlling the heating rate during thermal decomposition can produce Pt nanoparticles with specific sizes, such as coarse Pt particles with sizes of ≈60-160 nm consisting of PtNPs with dimensions of 1.9 and 4.1 nm.

The intensity of the Pt4f XPS signal does not directly scale with the nominal Pt loading, as the Pt4f signal from sample MP3 is relatively stronger than that of the other samples (Fig. 8), even of sample MP5.

This can be explained by the surface sensitivity of XPS of only a few nanometres. Although sample MP5 has a higher platinum concentration than sample MP3, the surface coverage of the PtNPs in sample MP3 is more uniform. As observed with SEM and TEM, the samples with lower Pt loadings have nanorods coated with a more uniform layer of oxidized Pt and small Pt(0) nanoparticles. For sample MP5, most of Pt has agglomerated in larger particles of 10–20 nm at the expense of the smaller particles that were uniformly coating the rods at lower Pt loading. This could leave parts of the surface of the MnO$_2$ rods bare of Pt, hence lowering the Pt surface coverage, thereby reducing the attenuation of the Mn2p signal. Also, this decreases the Pt4f signal when the Pt accumulates in larger 10–20 nm particles, of which only the top few nanometres are detected by XPS.

The investigation of the catalytic properties of the synthesized samples MP0, MP1, MP3, and MP5 was performed using the catalytic reduction of 4-nitrophenol to 4-aminophenol with NaBH$_4$. As previously mentioned, this reaction is generally used for testing the efficiency of various noble metal nanoparticles such as Pt, Pd, and Ag [13,18,43], therefore, the results of this study can be easily compared to the results obtained by other authors. However, it appears that the catalytic performance of Pt/MnO$_2$ for the reduction of 4-NP to 4-AP has never been studied. The reduction of 4-NP to 4-AP is an oxidation–reduction (redox) reaction in which the nitro group (–NO$_2$) of 4-NP is reduced to an amine group (–NH$_2$) of 4-AP.

The platinum-containing samples MP1, MP3, and MP5 completely catalytically reduced 4-NP to 4-AP after 3.5, 2.5, and 1.5 min, respectively. This can be seen from the disappearance of the maximum at 400 nm due to 4-NP and the appearance of a new maximum at 300 nm due to the formation of 4-AP. The more highly loaded sample showed higher catalytic activity (MP5 > MP3 > MP1). The catalytic activity of Pt on metal oxide supports depends on several factors, such as platinum loading, dispersion of platinum, availability of platinum on the surface, and interaction of platinum with reducible metal oxide supports. The best catalytic activity of the most highly loaded sample with 5 mol% Pt (sample MP5) can be explained simply by the high Pt loading.

However, this increase in k_{app} was not linear with Pt loading. The activity parameter, κ, or k_{app}/m_{Pt} (s^{-1} g^{-1}) better expresses the true catalytic efficiency of a sample as it normalizes the apparent rate constant with respect to catalyst mass. Some authors argue that the κ_c parameter, which takes both the mass of the catalyst and the reaction volume into account, is the most suitable value when comparing between studies. Considering this, we have calculated all three kinetic parameters of interest. The manganese oxide support was shown to be catalytically inactive; therefore, we have normalized the apparent rate constant with respect to Pt mass only (Table 3). It is evident that the sample with the smallest Pt loading, MP1, is the most efficient catalyst with the highest activity parameter of 1.8×10^4 s^{-1} g^{-1}. The highest mass-normalized rate constant of sample MP1, which as synthesized contains no Pt(0) but only Pt(II) and Pt(IV), strongly suggests that the presence of Pt(IV) is not a limiting factor for the catalytic reduction of 4-NP to 4-AP [44–47]. It should be noted that NaBH$_4$ present in the reaction mixture can reduce Pt(II) and Pt(IV) to Pt(0), but this does not seem to be so important considering that the catalytic reaction starts immediately, i.e., there is no induction time for the reduction of the oxidised Pt species. Another important factor is the smallest average size of the PtO$_x$ nanoparticles in sample MP1, which is reflected in the largest exposed surface area of the catalytically active sites, which is also confirmed by the BET analysis (see Supplementary Information, Fig. S14).

Recyclability is one of the most important properties of a catalyst. After five cycles, all three samples still completely catalytically reduced 4-NP to 4-AP, but as can be seen in Fig. 12, the catalytic reaction slowed down and the time to complete the reaction increased from about 3 min to 15 min for samples MP1 and MP3 and to about 10 min for sample MP5. For sample MP5, the k_{app} value decreased from 4.9×10^{-2} s^{-1} in the first cycle to 7.4×10^{-3} s^{-1} in the fifth cycle, which can still be
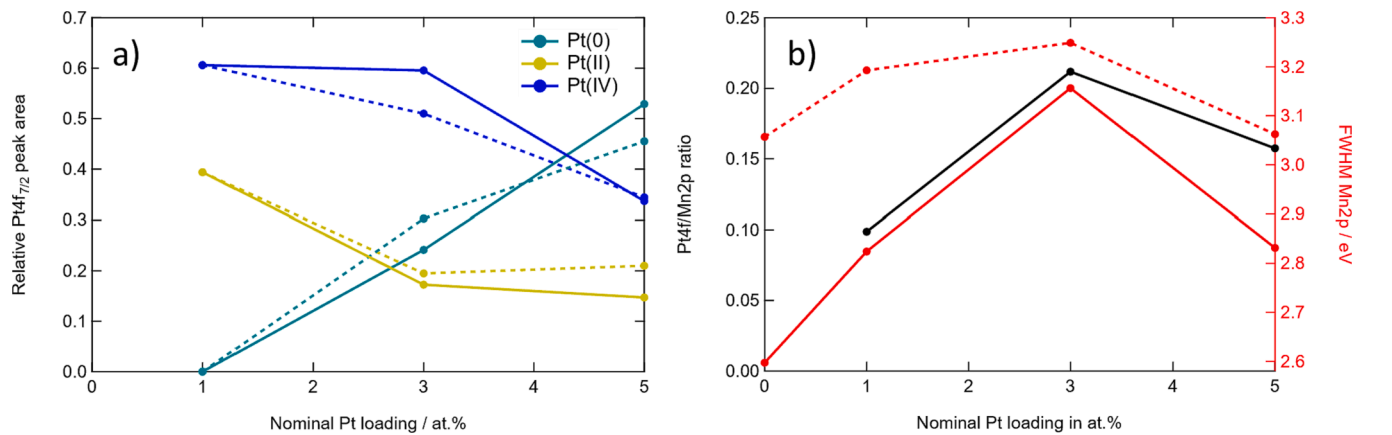
Fig. 8. Relative Pt4f$_{7/2}$ peak areas of the Pt(0), Pt(II), and Pt(IV) species (a). Fits for samples MP3 and MP5 were performed with two values (0.22, solid, and 0.12, dashed) for α (asymmetry parameter of the Doniach-Šunjić function to fit the Pt(0) species. Pt4f / Mn2p ratio (black) and Mn2p FWHM (red, 2p$_{3/2}$ solid and 2p$_{1/2}$ dashed) as a function of nominal Pt loading (b).
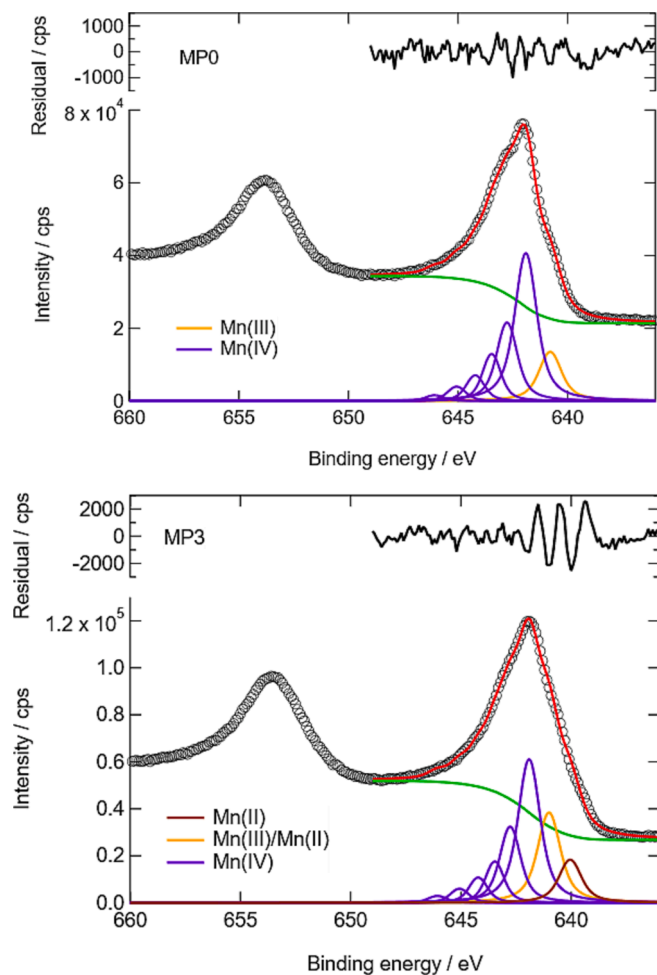

Fig. 9. Fitting of the Mn2p region of samples MP0 and MP3, according to the model proposed by Biesinger et al. [31].

Fig. 10. (a) Mn L$_{2,3}$ X-ray absorption spectra of samples MP0, MP1, MP3, and MP5 recorded in total electron yield. (b) Difference spectra of samples MP3 and MP5 with respect to the spectrum of sample MP0.

considered as efficient catalysts for the reduction of 4-NP to 4-AP. It is also important to note that the reduction in the k_{app} values was ~ 5 % lower for MP1 sample in comparison to MP3 and MP5 samples. It must be considered that NaBH$_4$ is in a 200-fold excess of 4-NP at the start of the reaction, but it is spent during catalytic cycles, as well as in reaction with atmospheric oxygen and oxidized Pt species. Therefore, we have
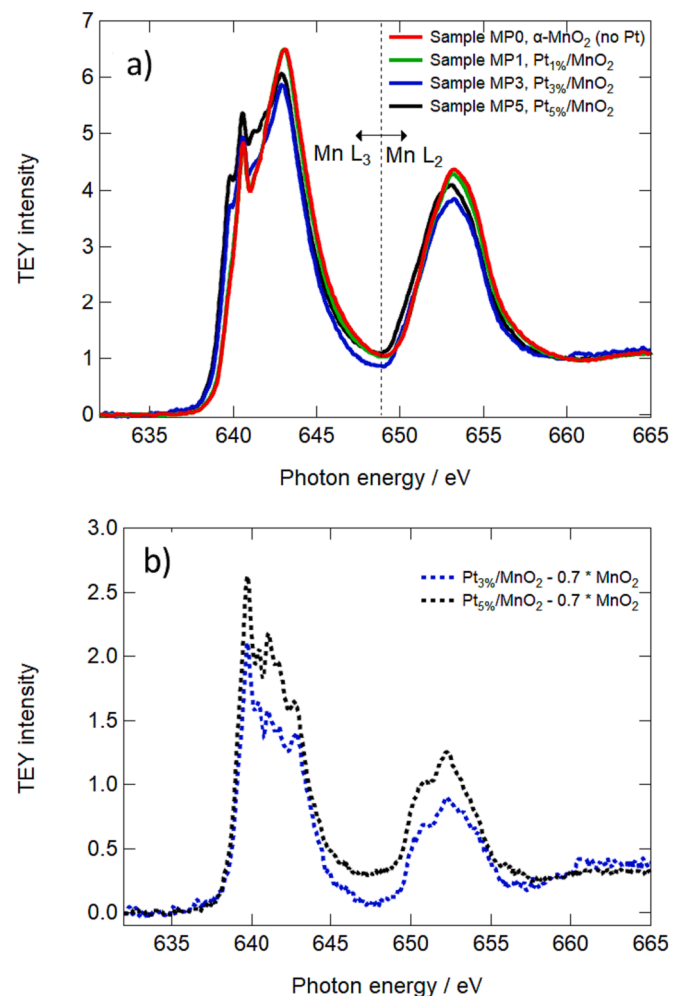
added another 200-fold excess of NaBH$_4$ prior to the third catalytic cycle in order to ensure its excess. However, it cannot be excluded that the variation in NaBH$_4$ could have retarded the k_{app} values of later catalytic cycles.

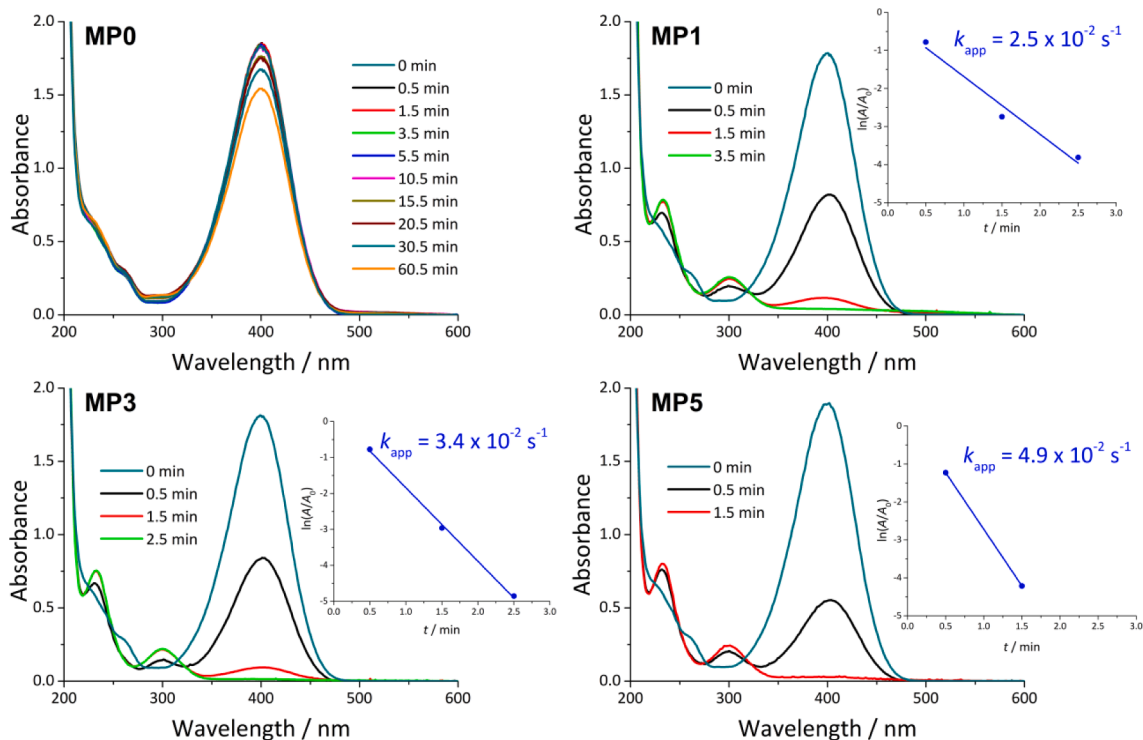Compared to other literature sources, the synthesized Pt/MnO$_2$ NRs

Fig. 11. Catalytic reduction of 4-nitrophenol (4-NP) to 4-aminophenol (4-AP) as a function of time for sample MP0, which contains no platinum, and samples MP1, MP3, and MP5, which contain around 1%, 3%, and 5% platinum, respectively. The insets show the calculated apparent rate constants assuming pseudo-first order kinetics.

Table 3

Calculated Pt mass in the catalyst samples (mass of all samples used in catalytic experiments was 0.06 mg), apparent rate constants k_{app}, and normalized constants, $k_{app}/m(Pt)$ and k_{app}/γ_{Pt} for samples MP1, MP3 and MP5. m represents the mass of Pt, while γ_{Pt} represents the mass concentration of Pt in the total volume of the catalytic reaction vessel.

Sample	m_{Pt} (g)	k_{app} (s^{-1})	k_{app}/m_{Pt} (s^{-1} g^{-1})	k_{app}/γ_{Pt} (L s^{-1} g^{-1})
MP1	1.4×10^{-6}	2.5×10^{-2}	1.8×10^{4}	53.8
MP3	4.0×10^{-6}	3.4×10^{-2}	8.5×10^{3}	25.5
MP5	6.7×10^{-6}	4.9×10^{-2}	7.3×10^{3}	21.9

have very high values of rate constants. Kharlamova *et al.* prepared CeO$_2$ with monometallic Pt and bimetallic Pt-Ag. In their work, the k_{app}/m_{Pt} values ranged from 0.73 to 46.78 46.78 s^{-1} g^{-1} [48]. In the work of Yang *et al.* in which they used anchored single atom Pt on carbon fibers, the highest k_{app}/m_{Pt} was 222.2 s^{-1} g^{-1} [49]. High activity Pt nanoparticles assembled on porous silica as shown in the work of Bogireddy *et al.* [50] exhibited k_{app} values on the same order of magnitude as the samples synthesized in our work. Pt/MnO$_2$ NRs synthesized in this work are highly active even compared to other noble metal catalysts, such as Pd@AuCu$_{nL}$ core shell nanocrystals [51], or Au nanoparticles synthesized by a "green" method [52], which exhibit k_{app} values in the order of 10^{-1} to 10^{-2} min^{-1}. Noh *et al.* [11] summarized various rate constants of a large number of supported Pt catalysts, and the comparison of our Pt/MnO$_2$ NRs with other Pt catalysts shows that our Pt/MnO$_2$ NRs are one of the most efficient Pt catalysts for the reduction of 4-nitrophenol (Table 3).

In many examples of Pt-based catalysts for the reduction of 4-NP [53], the particle size, morphology, and dispersion of Pt on the support are quite similar to the materials presented in this work, making the properties of Pt a crucial parameter, but not the only important one. It has been shown that the use of a suitable support is very important, and that the activity of metal nanoparticles can be increased up to 6-fold by using a favourable support [54]. MnO$_2$ alone catalyses the reaction very
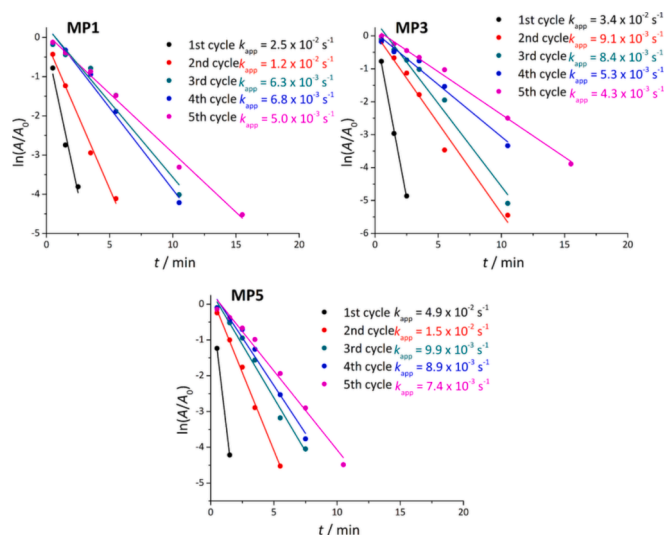

Fig. 12. Comparison of the apparent rate constants (k_{app}) and the recyclability of MP1, MP3 and MP5 samples during 5 catalytic cycles for the reduction of 4-NP to 4-AP.

poorly (Fig. 11), but its main advantage lies in its electron conductivity properties. These properties allow MnO$_2$ to serve as an electron relay from BH$_4^-$ to the substrate in addition to the electrons transferred from the nanoparticles, as argued by Bingwa *et al.* [54]. Moreover, the same authors suggested that hydrogen generated during the hydrolysis of BH$_4^-$ could spill over onto the metal oxide support and thus increase the rate of BH$_4^-$ hydrolysis, i.e., electron generation. In addition, there is evidence of the interaction of the manganese oxide support with Pt species on its surface, especially for the sample with the lowest Pt loading. Finally, the XPS spectra also show that there is no Pt(0) in MP1 sample,

but only Pt(II) and Pt(IV), shortened as PtO_x. It is plausible that these PtO_x species act as catalysts for the reduction of 4-NP to 4-AP similar to the metallic PtNPs.

5. Conclusions

In this study, homogeneous dispersion of platinum nanoparticles (PtNPs) on synthesized α-MnO$_2$ nanorods using Pt(II) acetylacetonate precursor was demonstrated. Platinum loading had a significant effect on the morphology and phase composition of the α-MnO$_2$ nanorods. The XRD, Raman and Mn L$_{2,3}$ edge NEXAFS results showed that Pt(acac)$_2$ played a crucial role in promoting the phase transition from α-MnO$_2$ to Mn$_5$O$_8$ (Mn$_2^{2+}$Mn$_3^{4+}$O$_8$). The SEM analysis showed that the PtNPs caused a decrease in the length of the α-MnO$_2$ nanorods. These results confirm the strong interaction of platinum with reducible α-MnO$_2$ support. Moreover, this study showed that the synthesized Pt/α-MnO$_2$ nanorods exhibited remarkable catalytic activity for the reduction of 4-NP to 4-AP. In particular, the sample with the lowest platinum content (sample MP1) exhibited the highest mass normalized rate constant k_{app}/m of 1.8×10^4 s^{-1} g^{-1}. Containing no Pt(0) but only Pt(II) and Pt(IV), as determined by XPS, this strongly suggests that the presence of Pt(IV) is not a limiting factor for the catalytic reduction of 4-NP to 4-AP. Overall, the results of this study indicate a strong interaction of homogeneously dispersed platinum on the α-MnO$_2$ nanorods, which could serve as highly efficient catalysts for the reduction of 4-NP to 4-AP and very likely for a variety of other catalytic applications.

CRediT authorship contribution statement

Ivan Marić: Investigation, Formal analysis, Data Curation, Writing - Original Draft, Writing - Review & Editing, Visualization. **Monika Šoltić:** Investigation, Data Curation, Formal analysis, Writing - Original Draft, Writing – Review & Editing. **Goran Dražić:** Investigation, Resources, Writing - Review and Editing. **Matthijs A. van Spronsen:** Investigation, Data Curation, Formal analysis, Writing - Original Draft, Writing – Review & Editing. **Goran Štefanić:** Formal analysis, Writing – original draft. **Mile Ivanda:** Investigation, Resources. **Georg Held:** Resources, Writing - Review & Editing. **Tanja Jurkin:** Resources, Writing – Review & Editing. **Klemen Bohinc:** Funding acquisition, Project administration, Resources. **Marijan Gotić:** Conceptualization, Methodology, Resources, Writing – Review & Editing, Supervision, Project administration, Funding acquisition.

Declaration of competing interest

The authors declare the following financial interests/personal relationships which may be considered as potential competing interests: [Dr. Matthijs A. Van Spronsen serves as a managing editor of Applied Surface Science. If there are other authors, they declare that they have no known competing financial interests or personal relationships that could have appeared to influence the work reported in this paper].

Data availability

Data will be made available on request.

Appendix A. Supplementary data

Supplementary data to this article can be found online at https://doi.org/10.1016/j.apsusc.2023.159091.

References

[1] D.D. Mal, D. Pradhan, Recent advances in non-noble metal-based oxide materials as heterogeneous catalysts for C-H activation, Dalton Trans. 51 (2022) 17527–17542, https://doi.org/10.1039/d2dt02613a.

[2] I.W. Davies, L. Matty, D.L. Hughes, P.J. Reider, Are heterogeneous catalysts precursors to homogeneous catalysts? J Am Chem Soc. 123 (2001) 10139–10140, https://doi.org/10.1021/ja016877v.

[3] Y. Ren, W. Xie, Y. Li, J. Ma, J. Li, Y. Liu, Y. Zou, Y. Deng, Noble metal nanoparticles decorated metal oxide semiconducting nanowire arrays interwoven into 3D mesoporous superstructures for low-temperature gas sensing, ACS Cent Sci. 7 (2021) 1885–1897, https://doi.org/10.1021/acscentsci.1c00912.

[4] X. Liu, J. Iocozzia, Y. Wang, X. Cui, Y. Chen, S. Zhao, Z. Li, Z. Lin, Noble metal-metal oxide nanohybrids with tailored nanostructures for efficient solar energy conversion, photocatalysis and environmental remediation, Energy Environ Sci. 10 (2017) 402–434, https://doi.org/10.1039/c6ee02265k.

[5] Y. Luo, C. Zhang, B. Zheng, X. Geng, M. Debliquy, Hydrogen sensors based on noble metal doped metal-oxide semiconductor: A review, Int J Hydrogen Energ. 42 (2017) 20386–20397, https://doi.org/10.1016/j.ijhydene.2017.06.066.

[6] W. Xiao, D. Wang, X.W. Lou, Shape-controlled synthesis of MnO$_2$ nanostructures with enhanced electrocatalytic activity for oxygen reduction, J. Phys. Chem. C. 114 (2010) 1694–1700, https://doi.org/10.1021/jp909386d.

[7] X. Yu, J. He, D. Wang, Y. Hu, H. Tian, Z. He, Facile controlled synthesis of Pt/MnO$_2$ nanostructured catalysts and their catalytic performance for oxidative decomposition of formaldehyde, J. Phys. Chem. C. 116 (2012) 851–860, https://doi.org/10.1021/jp208947e.

[8] F. Wang, H. Dai, J. Deng, G. Bai, K. Ji, Y. Liu, Manganese oxides with rod-, wire-, tube-, and flower-like morphologies: Highly effective catalysts for the removal of toluene, Environ Sci Technol. 46 (2012) 4034–4041, https://doi.org/10.1021/es204038j.

[9] H. Li, B. Fu, H. Huang, S. Wu, J. Ge, J. Zhang, F. Li, P. Qu, Catalytic degradation of organic pollutants by manganese oxides: A comprehensive review, Env. Pollut. Bioavail. 34 (2022) 395–406, https://doi.org/10.1080/26395940.2022.2123047.

[10] J.J. Shan, L. Nguyen, S. Zhang, F.F. Tao, Water-gas shift on Pd/α-MnO2 and Pt/α-MnO2, Catal Letters. 145 (2015) 1571–1580, https://doi.org/10.1007/s10562-015-1549-9.

[11] J. Noh, R. Meijboom, Reduction of 4-nitrophenol as a model reaction for nanocatalysis, Application of Nanotechnol. in Water Research. (2014) 333–405, https://doi.org/10.1002/9781118939314.ch13, 9781118496.

[12] R.D. Neal, R.A. Hughes, P. Sapkota, S. Ptasinska, S. Neretina, Effect of nanoparticle ligands on 4-nitrophenol reduction: Reaction rate induction time, and ligand desorption, ACS Catal. 10 (2020) 10040–10050, https://doi.org/10.1021/acscatal.0c02759.

[13] A.I. Ayad, D. Luart, A.O. Dris, E. Guénin, Kinetic analysis of 4-nitrophenol reduction by "water-soluble" palladium nanoparticles, Nanomater. 10 (2020) 1–16, https://doi.org/10.3390/nano10061169.

[14] A. Murugadoss, A. Chattopadhyay, A "green" chitosan-silver nanoparticle composite as a heterogeneous as well as micro-heterogeneous catalyst, Nanotechnol. 19 (2008) 015603, doi:10.1088/0957-4484/19/01/015603.

[15] I. Marić, M. Gotić, A. Pustak, G. Dražić, J.M. Grenèche, T. Jurkin, Magnetic δ-FeOOH/Au nanostructures synthesized using γ-irradiation method and their catalytic activity for the reduction of 4-nitrophenol, Appl. Surf. Sci. 611 (2023) 155653, https://doi.org/10.1016/j.apsusc.2022.155653.

[16] Y. Mei, G. Sharma, Y. Lu, M. Ballauff, M. Drechsler, T. Irrgang, R. Kempe, High catalytic activity of platinum nanoparticles immobilized on spherical polyelectrolyte brushes, Langmuir. 21 (2005) 12229–12234, https://doi.org/10.1021/la052120w.

[17] G.W. Qin, W. Pei, X. Ma, X. Xu, Y. Ren, W. Sun, L. Zuo, Enhanced catalytic activity of Pt nanomaterials: From monodisperse nanoparticles to self-organized nanoparticle-linked nanowires, J. Phys. Chem. C. 114 (2010) 6909–6913, https://doi.org/10.1021/jp910864w.

[18] S.K. Ghosh, M. Mandal, S. Kundu, S. Nath, T. Pal, Bimetallic Pt-Ni nanoparticles can catalyze reduction of aromatic nitro compounds by sodium borohydride in aqueous solution, Appl Catal A Gen. 268 (2004) 61–66, https://doi.org/10.1016/j.apcata.2004.03.017.

[19] L. Zhou, C. Gao, W. Xu, Robust Fe3O4/SiO2-Pt/Au/Pd magnetic nanocatalysts with multifunctional hyperbranched polyglycerol amplifiers, Langmuir. 26 (2010) 11217–11225, https://doi.org/10.1021/la100556p.

[20] H. Wang, K. An, A. Sapi, F. Liu, G.A. Somorjai, Effects of nanoparticle size and metal/support interactions in Pt-catalyzed methanol oxidation reactions in gas and liquid phases, Catal Letters. 144 (2014) 1930–1938, https://doi.org/10.1007/s10562-014-1347-9.

[21] J. Liu, R. Younesi, T. Gustafsson, K. Edström, J. Zhu, Pt/α-MnO$_2$ nanotube: A highly active electrocatalyst for Li-O$_2$ battery, Nano Energ. 10 (2014) 19–27, https://doi.org/10.1016/j.nanoen.2014.08.022.

[22] S. Huang, B. Cheng, J. Yu, C. Jiang, Hierarchical Pt/MnO$_2$-Ni(OH)$_2$ hybrid nanoflakes with enhanced room-temperature formaldehyde oxidation activity, ACS Sustain Chem Eng. 6 (2018) 12481–12488, https://doi.org/10.1021/acssuschemeng.8b03139.

[23] B. Unnikrishnan, P.L. Ru, S.M. Chen, Electrochemically synthesized Pt-MnO$_2$ composite particles for simultaneous determination of catechol and hydroquinone, Sens Actuators B Chem. 169 (2012) 235–242, https://doi.org/10.1016/j.snb.2012.04.075.

[24] M. Gotić, T. Jurkin, S. Musić, K. Unfried, U. Sydlik, A. Bauer-Šegvić, Microstructural characterizations of different Mn-oxide nanoparticles used as models in toxicity studies, J Mol Struct. 1044 (2013) 248–254, https://doi.org/10.1016/j.molstruc.2012.09.083.

[25] T. Gao, P. Norby, F. Krumeich, H. Okamoto, R. Nesper, H. Fjellvag, Synthesis and properties of layered-structured Mn$_5$O$_8$ nanorods, J. Phys. Chem. C. 114 (2010) 922–928, https://doi.org/10.1021/jp9097606.

[26] Y. Li, J. Wang, Y. Zhang, M.N. Banis, J. Liu, D. Geng, R. Li, X. Sun, Facile controlled synthesis and growth mechanisms of flower-like and tubular MnO$_2$ nanostructures by microwave-assisted hydrothermal method, J Colloid Interface Sci. 369 (2012) 123–128, https://doi.org/10.1016/j.jcis.2011.12.013.

[27] C. Du, S. He, X. Gao, W. Chen, Hierarchical Cu@MnO$_2$ core–shell nanowires: A nonprecious-metal catalyst with an excellent catalytic activity toward the reduction of 4-nitrophenol, ChemCatChem. 8 (2016) 2885–2889, https://doi.org/10.1002/cctc.201600567.

[28] S. Doniach, M. Sunjic, Many-electron singularity in X-ray photoemission and X-ray line spectra from metals, J. Phys. C Solid State Phys. 3 (1970) 285–291, https://doi.org/10.1088/0022-3719/3/2/010.

[29] C.R. O'Connor, M.A. van Spronsen, M. Karatok, J. Boscoboinik, C.M. Friend, M. M. Montemore, Predicting X-ray photoelectron peak shapes: The effect of electronic structure, J. Phys. Chem. C. 125 (2021) 10685–10692, https://doi.org/10.1021/acs.jpcc.1c01450.

[30] D.A. Shirley, High-resolution X-ray photoemission spectrum of the valence bands of gold, Phys Rev B. 5 (1972) 4709–4714, https://doi.org/10.1103/PhysRevB.5.4709.

[31] M.C. Biesinger, B.P. Payne, A.P. Grosvenor, L.W.M. Lau, A.R. Gerson, R.St.C. Smart, Resolving surface chemical states in XPS analysis of first row transition metals, oxides and hydroxides: Cr, Mn, Fe, Co and Ni, Appl Surf Sci. 257 (2011) 2717–2730, https://doi.org/10.1016/j.apsusc.2010.10.051.

[32] G. Held, F. Venturini, D.C. Grinter, P. Ferrer, R. Arrigo, L. Deacon, W. Quevedo Garzon, K. Roy, A. Large, C. Stephens, A. Watts, P. Larkin, M. Hand, H. Wang, L. Pratt, J.J. Mudd, T. Richardson, S. Patel, M. Hillman, S. Scott, Ambient-pressure endstation of the versatile soft X-ray (VerSoX) beamline at diamond light source, J Synchrotron Radiat. 27 (2020) 1153–1166, https://doi.org/10.1107/S1600577520009157.

[33] L. Lutterotti S. Matthies H.-R. Wenk Maud (material Analysis Using Diffraction): a User Friendly Java Program for Rietveld Texture Analysis and More, in 1999 NRC Research Press Ottawa Canada 1599.

[34] L. Lutterotti, Maud: A Rietveld analysis program designed for the internet and experiment integration, Acta Crystallogr A. 56 (2000) s54–s, https://doi.org/10.1107/S0108767300021954.

[35] H.M. Rietveld, The Rietveld method, Phys Scr. 89 (2014) 098002, https://doi.org/10.1088/0031-8949/89/9/098002.

[36] G.K. Williamson, W.H. Hall, X-ray line broadening from filed aluminium and wolfram, Acta Metall. 1 (1953) 22–31, https://doi.org/10.1016/0001-6160(53)90006-6.

[37] D.L. Bish J.E. Post eds. Modern Powder Diffraction Mineralogical Society of America 1989.

[38] G. Štefanić, S. Krehula, I. Štefanić, The high impact of a milling atmosphere on steel contamination, Chem. Commun. 49 (2013) 9245, https://doi.org/10.1039/c3cc44803g.

[39] T. Gao, M. Glerup, F. Krumeich, R. Nesper, H. Fjellvåg, P. Norby, Microstructures and spectroscopic properties of cryptomelane-type manganese dioxide nanofibers, J. Phys. Chem. C. 112 (2008) 13134–13140, https://doi.org/10.1021/jp804924f.

[40] B. Gilbert, B.H. Frazer, A. Belz, P.G. Conrad, K.H. Nealson, D. Haskel, J.C. Lang, G. Srajer, G. De Stasio, Multiple scattering calculations of bonding and X-ray absorption spectroscopy of manganese oxides, J Phys Chem A. 107 (2003) 2839–2847, https://doi.org/10.1021/jp021493s.

[41] X. Shan, D.S. Charles, Y. Lei, R. Qiao, G. Wang, W. Yang, M. Feygenson, D. Su, X. Teng, Bivalence Mn$_5$O$_8$ with hydroxylated interphase for high-voltage aqueous sodium-ion storage, Nat Commun. 7 (2016) 13370, doi:10.1038/ncomms13370.

[42] A.A. Kulbakov, M. Allix, A. Rakhmatullin, A.S. Mikheykin, Y.V. Popov, N. V. Smirnova, O. Maslova, I.N. Leontyev, In situ investigation of non-isothermal decomposition of Pt acetylacetonate as one-step size-controlled synthesis of Pt Nanoparticles, Physica Status Solidi (A) Applications and Mater. Sci. 215 (2018), https://doi.org/10.1002/pssa.201800488.

[43] C. Kästner, A.F. Thünemann, Catalytic reduction of 4-nitrophenol using silver nanoparticles with adjustable activity, Langmuir. 32 (2016) 7383–7391, https://doi.org/10.1021/acs.langmuir.6b01477.

[44] M.Y. Smirnov, E.I. Vovk, A.V. Nartova, A.V. Kalinkin, V.I. Bukhtiyarov, An XPS and STM study of oxidized platinum particles formed by the interaction between Pt/HOPG with NO$_2$, Kinet. Catal. 59 (2018) 653–662, https://doi.org/10.1134/S0023158418050129.

[45] M.Y. Smirnov, E.I. Vovk, A.V. Kalinkin, P.A. Simonov, E.Y. Gerasimov, V. I. Bukhtiyarov, Formation of surface platinum oxides in the interaction of the Pt/Sibunit catalysts with NO$_2$: Estimates of the width of oxide shell from XPS data, Kinet. Catal. 59 (2018) 663–671, https://doi.org/10.1134/S0023158418050130.

[46] S. Steinhauer, E. Lackner, F. Sosada-Ludwikowska, V. Singh, J. Krainer, R. Wimmer-Teubenbacher, P. Grammatikopoulos, A. Köck, M. Sowwan, Atomic-scale structure and chemical sensing application of ultrasmall size-selected Pt nanoparticles supported on SnO$_2$, Mater Adv. 1 (2020) 3200–3207, https://doi.org/10.1039/d0ma00244e.

[47] A.V. Kalinkin, M.Y. Smirnov, V.I. Bukhtiyarov, Oxidation of a platinum foil with nitrogen dioxide, Kinet. Catal. 57 (2016) 826–830, https://doi.org/10.1134/S0023158416060069.

[48] T.S. Kharlamova, M.V. Salina, V.A. Svetlichnyi, M.A. Salaev, A.I. Stadnichenko, G. V. Mamontov, CeO$_2$-supported Pt–Ag bimetallic catalysts for 4-nitrophenol reduction, Catal Today. 384–386 (2022) 12–24, https://doi.org/10.1016/j.cattod.2021.08.031.

[49] X. Yang, J. Wang, Y. Wei, B. Li, W. Yan, L. Yin, D. Wu, P. Liu, P. Zhang, Cotton-derived carbon fiber-supported Ni nanoparticles as nanoislands to anchor single-atom Pt for efficient catalytic reduction of 4-nitrophenol, Appl. Catal. A. Gen. 643 (2022) 118734, https://doi.org/10.1016/j.apcata.2022.118734.

[50] N.K.R. Bogireddy, P. Sahare, U. Pal, S.F.O. Méndez, L.M. Gomez, V. Agarwal, Platinum nanoparticle-assembled porous biogenic silica 3D hybrid structures with outstanding 4-nitrophenol degradation performance, Chem. Eng. J. 388 (2020) 124237, https://doi.org/10.1016/j.cej.2020.124237.

[51] S.K. Krishnan, R. Esparza, D.B. Uribe, S. Mukherjee, U. Pal, Facile seed-mediated growth of ultrathin AuCu shells on Pd nanocubes and their enhanced nitrophenol degradation reactions, J. Phys. Chem. C. 125 (2021) 13759–13769, https://doi.org/10.1021/acs.jpcc.1c00646.

[52] N.K.R. Bogireddy, U. Pal, L.M. Gomez, V. Agarwal, Size controlled green synthesis of gold nanoparticles using Coffea arabica seed extract and their catalytic performance in 4-nitrophenol reduction, RSC Adv. 8 (2018) 24819–24826, https://doi.org/10.1039/c8ra04332a.

[53] I. Marić, G. Dražić, E. Radin, R. Peter, M. Škrabić, T. Jurkin, A. Pustak, N. Baran, L. Mikac, M. Ivanda, M. Petravić, G. Štefanić, M. Gotić, Impact of platinum loading and dispersion on the catalytic activity of Pt/SnO$_2$ and Pt/α-Fe$_2$O$_3$, Appl Surf Sci 607 (2023) 155073, https://doi.org/10.1016/j.apsusc.2022.155073.

[54] N. Bingwa, R. Patala, J.H. Noh, M.J. Ndolomingo, S. Tetyana, S. Bewana, R. Meijboom, Synergistic effects of gold-palladium nanoalloys and reducible supports on the catalytic reduction of 4-nitrophenol, Langmuir. 33 (2017) 7086–7095, https://doi.org/10.1021/acs.langmuir.7b00903.